

# Finite Element Modeling of Pneumatic Bending Actuators for Inflated-Beam Robots

Cosima du Pasquier, Sehui Jeong, and Allison M. Okamura, *Fellow, IEEE*

**Abstract**—Inflated-beam soft robots, such as tip-everters vine robots, can control their curvature by contracting one side of the beam using pneumatic actuation. In this work, a general finite element modeling approach is developed and applied to characterize bending of inflated-beam soft robots. The model is tested on four types of pneumatic actuators used in these robots (series, compression, embedded, and fabric pneumatic artificial muscles) and can be extended to other designs. Actuators rely on two types of bending mechanisms: geometry-based contraction and material-based contraction. Geometry-based contraction implies shape-change of the muscles from a flat to an inflated shortened configuration that causes buckling of the inflated beam. Material-based contraction relies on material anisotropy to produce a contraction effect. The model depicts both mechanisms and accommodates for the complex and highly nonlinear effects of buckling and anisotropy. Simulation results are verified experimentally for each actuator type at three working pressures (10, 20, and 30 kPa). Geometry-based contraction achieves the largest deformation at accuracy values of 92.1% and higher once the buckling pattern is established, and 80.7% and higher for lower pressures due to the stress singularities occurring with buckling formation. Material-based contraction achieves smaller bending angles but is at least 96.7% accurate. The models are freely available online, and can thus be used by others to design inflated-beam robots, such as tip-everters vine robots. Labor and material waste can be reduced with this tool by optimizing designs that use knowledge of material properties and stress to distributions to enable bending and manage stress peaks.

**Index Terms**—Inflated-Beam Robots, Pneumatic Actuation, Explicit FEA, Anisotropic Material Model

## I. INTRODUCTION

SOFT robotic systems are developed and adopted for safe physical interaction with complex or delicate environments. In contrast to their rigid counterparts, control of soft robots is achieved through embedded design features, such as actuators or pleats, that inherently link form to function [1]. Typically, lengthy iterative experimentation has been used to refine the design features of soft robotics. However, finite element (FE) modeling and analysis have been shown to support automated design optimization and performance prediction, significantly reducing the material and time cost of building a new soft robot while ensuring that it operates within safe and reliable limits [2], [3].

Inflated beam robots (IBRs) are a class of soft robots that use pressurized textile or plastic sleeves to achieve a range of shapes and access constrained or cluttered environments [4], [5], [6]. They possess a large number of degrees of freedom (DoFs) that can be controlled through pleats [7], internal devices [8], [9], tendons [4], [10], and pneumatic actuators [11], [12], [13].

Tip-everters inflated beam robots, also called vine robots,

are a subclass of IBRs in which the beam wall material is initially inverted inside the robot. Pressure-driven eversion causes the vine robot to “grow”, extending its tip while the beam wall is stationary relative to its environment. This is advantageous for applications with delicate environments to be navigated via tortuous paths, like surgery, search and rescue, and archaeology [11], [14]. However, mechanisms to control beam bending are constrained by the limited space within the sleeve and by the eversion process. This has motivated the design of a range of pneumatic actuators placed on the beam surface. These actuators can be stowed flat during eversion and then inflated to control the deployed beam’s shape [15]. Past work on modeling of pneumatic actuators for bending IBRs has focused on kinematics and relied on geometrical approximations of volume change, virtual work, and conservation of energy [13], [16], [17]. These models only offer a rough approximation of the deformed center axis of the IBR. Pneumatic actuators rely either on geometry-based contraction or material-based contraction to generate bending. Geometric contraction causes distributed buckling throughout the beam, a complex process sensitive to small fluctuations in pressure that is dependent on the material and stress distribution in the beam, two qualities missing from kinematic modeling. Material-based contraction relies on material anisotropy that entirely depends on shear stress distribution, which is also not captured by kinematic modeling. Thus, existing models can only approximate deformation through iterative parametric tuning based on experimental data, which requires time-intensive prototyping and testing procedures. Each change in design or material requires a new tuning process.

In contrast, finite element modeling (FEM) captures internal forces, strains, and stresses, and can predict both buckling and anisotropy. Although FEM requires initial material characterization and mesh refinement as part of the model setup, it can then accommodate changes in geometry and material. Exterior loads, such as those encountered when interacting with an object in the environment, can be seamlessly integrated into the same model.

In this work, we propose the first general FE framework for predicting the deformation of pneumatically actuated IBRs, encompassing both buckling and anisotropic bending mechanisms. The constitutive models for quasi-isotropic and inextensible materials used for buckling and anisotropic extensible materials used for anisotropy are integrated into the FE software Abaqus CAE [18]. By utilizing *Dynamic, Explicit*<sup>1</sup>

<sup>1</sup>Abaqus CAE-specific functionalities are capitalized and italicized throughout the text.

FE analysis, our data-driven model predicts deformation in IBRs for four main types of pneumatic actuators: series, compression, fabric, and embedded pneumatic artificial muscles (sPAMs [11], cPAMs [19], fPAMs [12], ePAMs [17]). sPAMs are also referred to in literature as series Pouch Motors, so we refer to them here as sPAMs/PMs [13]. We provide the FEA models freely online (<http://www.vinerobots.org>). The models can be modified to simulate and verify the bending modes of other pneumatic actuators for IBRs, to streamline their design and fabrication.

This paper is organized as follows: first, we describe the material mechanical characterization protocol and the benchmark experimental bending protocol for the four types of actuators. Then, we explain the assumptions for the FE model to efficiently mimic the experimental setup. We define the comparison metrics and error calculations used to establish the validity of the FE models. Next, we present the experimental and simulation bending results and discuss the validity and robustness of our approach. Finally, we discuss the results in the wider context of pneumatic actuation of IBRs.

#### A. Background

##### 1) Modeling of Deformation in Pneumatically Actuated IBRs

Controlling an IBR with pneumatic actuators is more complex than with other mechanisms such as internal devices [8] or tendons [4] because the relationship between actuation and shape cannot be directly extrapolated from finite orientation or length changes. Differences between the bending mechanisms of pneumatic actuator types also influence how they are modeled.

Pneumatic actuators shorten a side of an IBR to generate bending, which can be achieved in two ways: through geometry-based contraction, where the transition from flat to 3D inflated configurations shortens the actuator, and through material anisotropy, where the inherent material properties cause the actuators to shorten.

The sPAM/PM, cPAM, and ePAM bending actuators all bend through geometry-based contraction. In the literature, they are typically modeled using conservation of energy and principle of virtual work [16], [17], [19], [20]. The analytical models describe the geometric changes of the actuators as they inflate, and equate the work done by the pressure to that of the virtual translation or contraction. They assume material inextensibility, constant curvature, and idealized linear spring behavior. Niiyama et al. [13] and Greer et al. [20] model sPAMs/PMs separately from the IBR body and for low pressures. Kübler et al. [19] model sPAMs/PMs and cPAMs including curvature and show promising results, but the accuracy varies with actuator dimensions. Abrar et al. [17] model bending of ePAMs, but the model and the experimental data differ significantly.

fPAMs achieve bending through material anisotropy. Nacleiro and Hawkes [12] model the actuator contraction by relating increase in pressure to increase in volume, based on existing models for McKibben muscles. Ultimate tensile strength is used to determine maximum pressure and maximum actuator contraction. The model performs very well for pure linear displacement of isolated actuators. Kübler et al. [19] extend

the model to bending by including the reaction forces between the IBR and the actuators in the equilibrium equations.

For both geometry-based contraction and material-based actuator contraction, the analytical models are actuator-specific and are tuned using experimental data. They do not provide stress and strain fields in the IBR, and thus are purely geared towards shape prediction and do not consider the full range information required for actuator design and fabrication.

##### 2) Static vs. dynamic FEA of thin-walled structures

The body of an IBR is a thin-walled cylindrical shell. The actuators on or in the body surface generate asymmetric lateral loading, which in turn causes the cylinder to bend through buckling. This specific scenario has not been documented in literature for FE analysis, but there is a body of literature concerning loading of thin-walled cylindrical shells under uniform lateral pressure [21], [22].

There are two methods to solve dynamic buckling FE problems with ABAQUS: *Standard* and *Explicit*. They use two different approaches to solving the general equilibrium equations in a structure:

$$\mathbf{M}\ddot{\mathbf{u}} + \mathbf{D}\dot{\mathbf{u}} + \mathbf{K}\mathbf{u} = \mathbf{F}, \quad (1)$$

where  $\mathbf{M}$  is the mass matrix,  $\mathbf{D}$  is the damping matrix,  $\mathbf{K}$  is the stiffness matrix,  $\mathbf{F}$  is the external load vector, and  $\mathbf{u}$  is the nodal displacement vector.

*ABAQUS/Standard* solves the equations implicitly using the Newton-Raphson method to iteratively converge towards a stable solution. The solution at time step  $t + \Delta T$  depends on the solution at time step  $t$ , and the process requires for  $\mathbf{K}$  to be recalculated at each step for the newly deformed structure.

*ABAQUS/Explicit* integrates the general equilibrium equations using the central difference formula at time step  $t$  directly from the previous time step without iterating towards an equilibrium. This approach is inherently less stable than *ABAQUS/Standard*, so the time step size needs to be adjusted to ensure correct results. A solution is considered valid if the kinetic energy of the system stays beneath 10% of the total internal energy [18].

Comparative studies have used both methods to model the buckling of thin-walled cylinders and have found that *ABAQUS/Explicit* achieves the same level of accuracy but at a fraction of the computational effort [21], [22]. We will thus use the *Explicit* approach to model the effect of bending actuators on IBRs.

## II. METHODS

In this section, we introduce the modeling approach and parameters for the FE model of IBRs that is derived from previous work modeling thin-walled structures. We explain the materials used for each actuator, and include the data acquisition methods used to estimate the constitutive material models. Then, we outline the actuator designs, assembly methods, and experimental protocol to evaluate their performance.

#### A. FE Model for IBRs

An FE model was built using Abaqus CAE *Explicit* to predict the deformation and reaction forces within the IBRs and respective actuators. The *Dynamic, Explicit* step was used since the IBR bending mechanism relies primarily on buckling,

which is not captured by *Quasi-Static, Standard* steps. For computational efficiency, the IBR and actuator models were defined as shells of thickness 200  $\mu\text{m}$  and 50  $\mu\text{m}$  for the TPU-coated and silicone-coated fabrics, respectively. In all four cases, the IBR and actuator mesh sizes were 4 mm and 1 mm respectively, which represents roughly 1% of the IBR length and 1.7% of a single actuator length. These sizes were chosen for their relative convergence accuracy and computational efficiency.

The model for the cPAM and ePAM actuators was built using *Tie* constraints at all the surfaces that were welded, and the sPAM/PM was built using the same *Tie* constraints for both welded and glued surfaces. For the fPAM, since the material and the glue have different elastic properties, the glued surface was modeled as a *Composite* surface combining the silicone-coated Nylon material properties and those of the glue. *General Contact* was defined to avoid collisions, and a 0.01 mm gap was introduced in between the IBR and actuator layers to allow the model to start without collision ambiguity.

A maximum pressure of 2kPa was applied to the IBR, and a maximum pressure of 10, 20, and 30 kPa was applied to all actuator interiors. The IBR pressure was applied in the first 0.1 seconds and then held, then the actuator pressures were applied for the remaining 1 second using two distinct *Smooth Amplitudes*. The total time of 1.1 seconds was chosen to minimize computational effort while keeping the kinetic energy of the model under 1% of the total energy. To avoid inertial effect and to ensure that steady-state deformation has been reached, each maximum pressure is simulated separately.

Both *Pinned* and *Encastered* boundary conditions (BCs) were tested. The change did not affect the results, so pinned BCs were applied to the final simulations.

#### B. Material Characterization

The sPAM/PM, cPAM, and ePAM all rely on geometric shape change for contraction, and thus require a sturdy inextensible material. We chose a 70D TPU-coated Ripstop Nylon because it easily bonds to itself when the coating is heated, which we achieve through ultrasonic welding, and it does not rip at the current working pressures. The fPAM relies on material anisotropy for contraction. We chose a silicone-coated Ripstop Nylon because of its proven anisotropic behavior in previous work [12]. The material properties needed for FEA were measured using uniaxial testing to break on an Instron 5565 under ASTM D882 measurement standard and rectangular test specimens. Five specimens were tested per material and per relevant orientation. The measured elastic moduli for the Nylon and the silicone fabrics are shown in Table I for each orientation.

In the experiments, the sPAM/PM, cPAM, and ePAM and their respective IBRs are all cut along the main axes of the textile (0° and 90°). The *Material Evaluation* module on Abaqus CAE was used to fit the 0° and 90° uniaxial test data of the TPU-coated Nylon to the *Reduced Polynomial* hyperelastic constitutive model with  $N = 1$ , where  $U = C_{10}(\bar{I} - 3)$ , resulting in the following material parameters:  $C_{10} = 50.3$ ,  $D_{10} = 0$ .

The main axis of the fPAM is cut at 45°, because the actuation mechanism relies on anisotropy for the fPAM to

TABLE I  
ELASTIC MODULI FOR BOTH MATERIALS USED TO FABRICATE FOUR TYPES OF IBR ACTUATORS.

Material	$E_0$	$E_{45}$	$E_{90}$
TPU-coated Nylon, Quest Outfitters	215 MPa	-	201 MPa
Silicone-coated Nylon, Rockywoods SCA	96.5 MPa	4.05 MPa	120 MPa

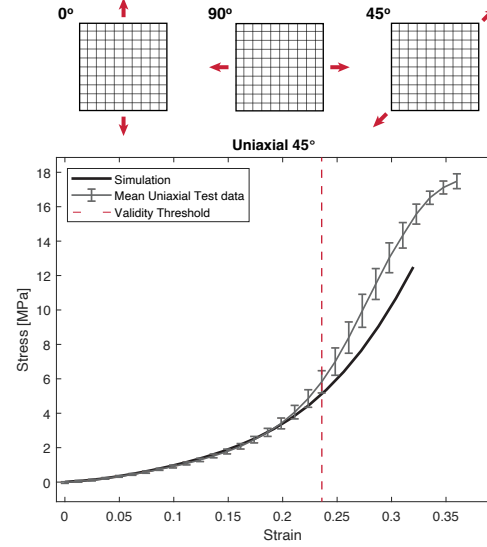


Fig. 1. Top: uniaxial loading orientations; bottom: stress-strain curve for Silicone-coated TPU; the simulation data in black matches the test data until a validity threshold of roughly 24% strain.

contract and cause the IBR to bend. The anisotropic material properties of the silicone-coated Nylon were modeled using the built-in *\*Fabric* material model in ABAQUS/Explicit. *\*Fabric* is a data-based model that uses uniaxial test data along the fill and warp directions of a fabric, and its shear response. The experimental data acquired as described above was thus implemented directly into Abaqus for the fill and warp directions (0° and 90°). The shear stress-strain curve was calculated by using the 45° uniaxial test data as a bias-extension test data (a common alternative to the picture-frame test) [23], [24]. At the center of the test specimens, the material is in pure shear and the shear angle is directly related to  $d$ , the displacement during the uniaxial test:

$$\gamma = \frac{\pi}{2} - 2 \arccos \left( \frac{L_0 + d}{\sqrt{2}L_0} \right), \quad (2)$$

where  $L_0$  is the initial specimen length. The shear force can be fit to uniaxial test data by relating it to the shear angle and  $d$  using the following equation:

$$F_{sh}(\gamma) = \frac{1}{(2H - 3W) \cos \gamma} \left( \left( \frac{H}{W} - 1 \right) \cdot F \cdot \left( \cos \frac{\gamma}{2} - \sin \frac{\gamma}{2} \right) - W \cdot F_{sh} \cdot \left( \frac{\gamma}{2} \right) \cdot \cos \frac{\gamma}{2} \right), \quad (3)$$

where  $H$  and  $W$  are dimensions of the sample along and across loading-direction respectively, and  $F$  is the external load applied during the uniaxial test. The fitting results are

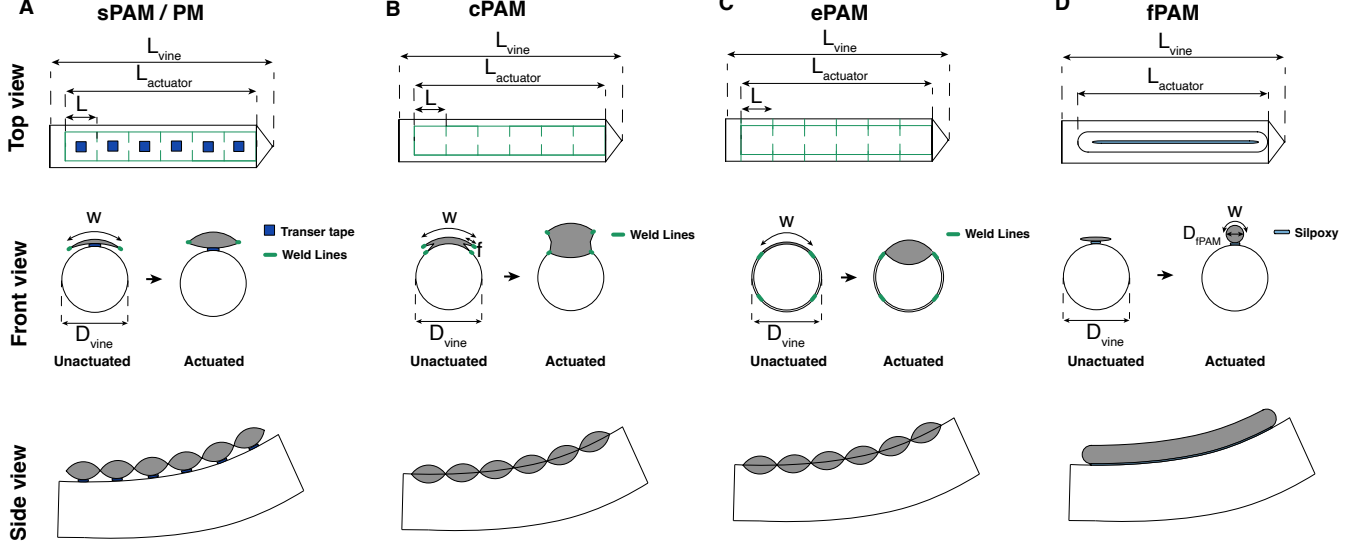


Fig. 2. Inflated beam robot (IBR) fabrication and dimensions overview; top to bottom: schematic top, front, and side view (actuated) and main dimensions for A. series pneumatic artificial muscle/pouch motor (sPAM/PM), sides welded over two layers and taped onto the IBR, B. compression pneumatic artificial muscle (cPAM), sides welded over four layers and directly onto the IBR, C. embedded pneumatic artificial muscle (ePAM), two cylinders welded in a pattern to integrate the actuator in the IBR surface, D. fabric pneumatic artificial muscle (fPAM), glued using Silpoxy.

shown in Fig. 1. The model matches the  $45^\circ$  test data well up to roughly 24% strain; values beyond that differ due to the assumption of thread inextensibility. Since the material is not strained beyond 24% in the fPAM tests, the model is valid.

#### C. Actuator Designs and Mechanisms

The IBR and actuator dimensions were chosen to be as similar as possible so the main differentiation between the four experiments is the actuation mechanism. The dimensions are given in Table II, and the design, bonding method, actuation method, and physical prototypes are shown in Fig. 2. The fabrication steps followed previous work (sPAM/Pouch Motors [13], cPAM [15], ePAM [17], fPAM [12]). For the sPAM/PM and the fPAM, the actuators are fabricated separately from the IBR body and then attached using adhesive transfer tape (3M, Saint Paul, Minnesota, United States) and Silpoxy adhesive (Reynolds Advanced Materials, Broadview, Illinois, United States) respectively. For the cPAM and the ePAM, the actuators are integrated on the surface of the IBR. The cPAMs are three layers of fabric selectively welded to create a form of origami pouch that unfolds under pressure. The ePAMs are created by selectively welding two parallel cylindrical IBR bodies into an actuation pattern. All four mechanisms are shown in the Front view of Fig. 2.

TABLE II  
DIMENSIONS FOR THE SPAM/PM, CPAM, EPAM, AND FPAM DESIGNS.

	sPAM/PM	cPAM	ePAM	fPAM
L <sub>IBR</sub>	360 mm	360 mm	360 mm	360 mm
D <sub>IBR</sub>	80 mm	80 mm	80 mm	80 mm
L <sub>actuator</sub>	60 mm	60 mm	60 mm	300 mm
W	360 mm	360 mm	360 mm	360 mm

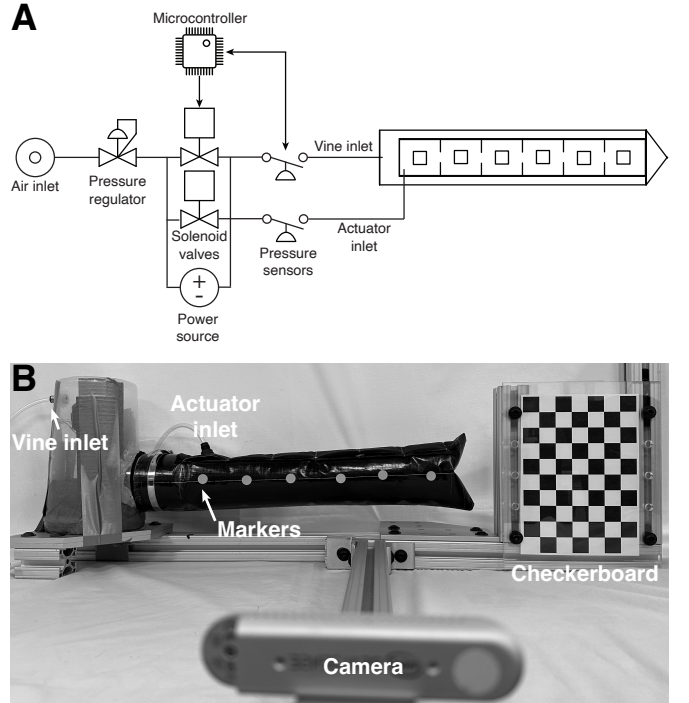


Fig. 3. Experimental setup: A. schematic pressure control system; B. IBR displacement measurement setup, including both air inlets (left), camera (middle front), and checkerboard (right) for measurement calibration; white dots show the six markers used for displacement measurement.

#### D. Experimental Evaluation

The experimental setup used to capture bending of the IBR and actuators is shown in Fig. 3. The control system, in Fig. 3A, is attached to a wall pressurized air inlet regulated manually to 100 kPa. The air is then split into two QB3 solenoid valves

TABLE III  
ACCURACY OF FE MODEL FOR THE  
SPAM/PM, CPAM, EPAM, AND FPAM ACTUATORS

	10 kPa	20 kPa	30 kPa
sPAM/PM	96.4%	95.8%	94.3%
cPAM	87.1%	97.0%	97.3%
ePAM	80.7%	92.1%	94.9%
fPAM	97.6%	97.3%	96.7%

that regulate pressure through digital sensors placed close to the IBR and the actuators. A microcontroller (Arduino Uno) records the pressure measurements to the valves and controlled the valves based on a predetermined test sequence. An Intel Realsense D145 camera captures RGB and depth images, using a checkerboard for calibration. Six markers placed along the IBR and at the height of the middle of each actuator pouch are used to measure displacement. The data acquired by the camera is post-processed using Python and plotted using Matlab.

Previous work showed that gravity has only a negligible effect on the measurements due to the light weight of the materials used in these experiments. The experimental and simulation setup are otherwise built to be as physically similar as possible.

Each actuator type was tested using the protocol below:

- 1) IBR pressurized at 2 kPa
- 2) Actuator sequentially pressurized to 10, 20, and 30 kPa consecutively for 5 seconds each
- 3) Actuator depressurized for 5 seconds

The 5-second duration for the inflation and deflation allow for the pressure in the actuators to achieve steady-state, which provides a more accurate reading of the pressure/displacement relationship. It is also close to what the FE procedure simulates, where each pressure is simulated and held to a threshold to avoid inertial effects.

#### E. Metrics

The finite element model and experimental displacement data are compared based on the XY-displacement of the markers. First, using a *Path* along the center line of the body of the IBR, the XY displacement coordinates vs. pressure are extracted from the output database (ODB) of the simulations. They are then plotted against the measured marker displacements at  $P = 10, 20, 30$  kPa, using the pressures measured at the inlet for the actuators and the final simulation pressure. The accuracy is calculated as one minus the least square error between the marker positions ( $y_{\text{EXP}}$ ) and the simulation displacement curve ( $y_{\text{FEA}}$ ):

$$a = 1 - \frac{1}{N_{\text{markers}}} \sum_{n=1}^{N_{\text{markers}}} \left( \frac{y_{\text{FEA}} - y_{\text{EXP}}}{y_{\text{FEA}}} \right)^2 \quad (4)$$

### III. RESULTS AND DISCUSSION

In this section, we first compare experimental and FEA results for individual actuators, then compare the actuators to each other. We discuss differences bending mechanisms, bending

range, and their effect on the accuracy of the simulation. We discuss the FEA strategy and its implications for the results. Finally, we analyze how the FEA presented in this work contributes to the fields of IBRs and Soft Robotics in terms of design and control.

The results for each actuator are shown in Fig. 4, and FEA accuracy values are given in Table III. Starting with the sPAM (Fig. 4.A), the experimental and simulation data correspond very well, with a minimum accuracy of 94.3%. The actuators are external to the IBR body so their axis of contraction is further away from the IBR central axis, which in turn limits the bending radius. The actuator location also implies that the IBR cross-section is affected very little by bending. The stress peaks, very similar in location and magnitude to those of the ePAM, are at the weld seams. The buckling pattern is irregular compared to the cPAM and ePAM, which indicates that the effect of external actuators is less evenly distributed and limits the bending range.

The cPAM (Fig. 4.B) exhibits the most displacement and strongest curvature. Embedded at the surface, the cPAMs are closer to the center axis of the IBR than the sPAMs and fPAM. The extra fold of fabric increases their expansion compared to the ePAMs, as signified by the actuator cross-section that has the largest actuator to IBR ratio. The effect of the folds is visible in the dual buckling pattern: one type of buckle appears in between the actuators, similar to the pattern of the ePAM, and the other at the actuator itself. The stress peaks are also at the weld lines, especially where four fabric layers connect. The FEA accuracy of the cPAM exceeds 97% for pressures over 20 kPa but sinks by 10% for lower pressures. The appearance of buckles causes stress singularities in the model. It is an inherently unstable mechanism that causes sudden large changes in bending. At 10 kPa, when the buckling pattern is only partially formed, the deformation is unstable and very sensitive to small variations in pressure. To support this hypothesis, we show the cPAM deformation at 11, 12, and 13 kPa in Fig. 5. A pressure difference of 3 kPa increases the maximum vertical displacement by nearly 30%. Given that the experimental setup includes a margin of error for pressure control, this explains the lower accuracy at 10 kPa.

The ePAM (Fig. 4.C) combines bending elements from the sPAM and cPAM. The deformed actuator shape is the same as the sPAM/PM, and, as for the cPAM, the actuators are embedded directly on the IBR and rely on a regular buckling pattern to deform. The displacement range of the ePAM thus lies between the two other actuator types. Since the bending mechanism is the same as the cPAM, the same stress singularities are found at low pressures (<20 kPa) and partially buckled states. Although the ePAMs are slightly less accurate than the cPAMs in our experiments, we should note that the fabrication of ePAMs is much more straightforward since it only involves welding two surfaces (no extra folds), and they can easily be combined on the IBR surface for 3D control.

Finally, the fPAM (Fig. 4.D) has the smallest bending range of the four, given that the bending mechanism relies solely on material contraction and that the actuator axis is furthest away from the IBR center axis. However, the bending mechanism is

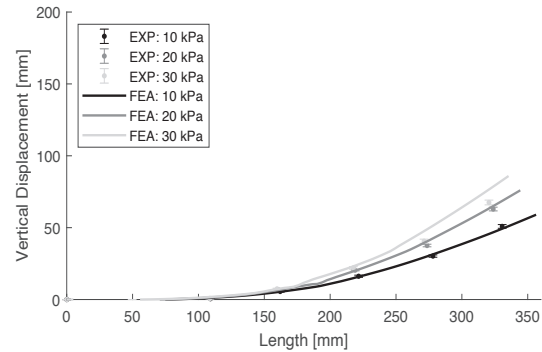
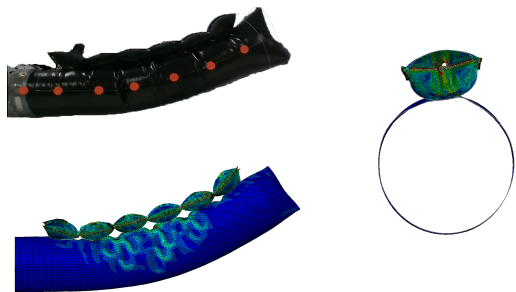
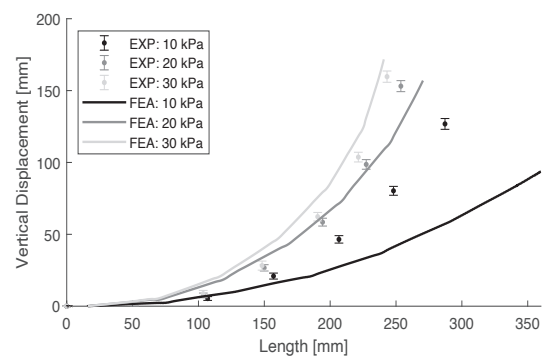
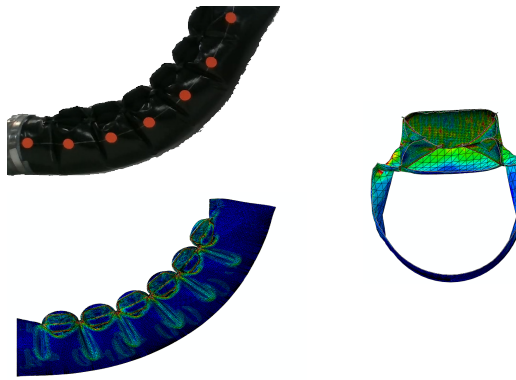
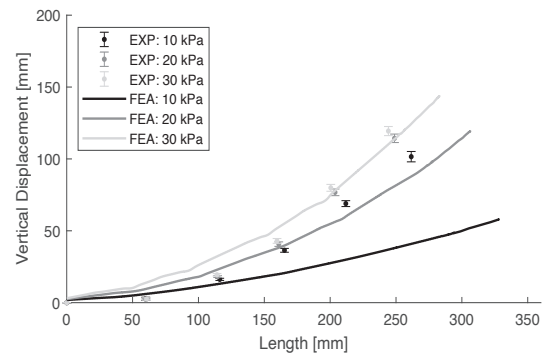
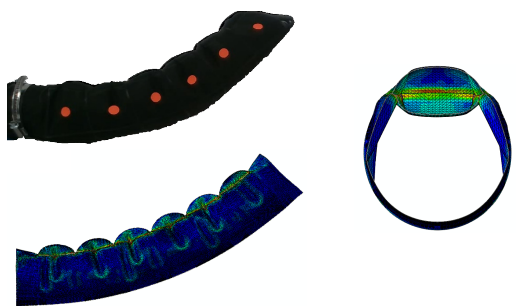
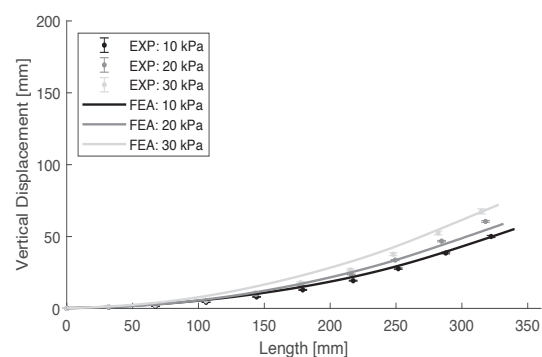
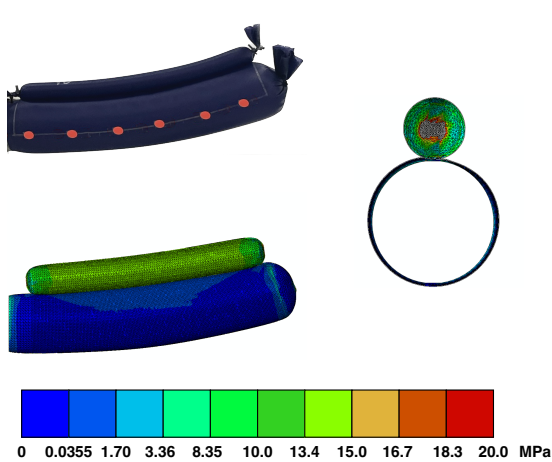
**A sPAM / PM****B cPAM****C ePAM****D fPAM**

Fig. 4. Results and comparison of experimental and FEA results for the four actuator types; in each actuator section there is a photograph of the actuator at 30 kPa (top, left), a capture of the von Mises Stress in FEA at 30 kPa from the side and a cross-section (center), and a graph comparing the displacements of the experiments (mean) and FEA in length and height at 10, 20, and 30 kPa (right); the experimental error bar represents the variation from the mean; the stress scale at the bottom is the same for all FEA results and capped at 20 MPa.

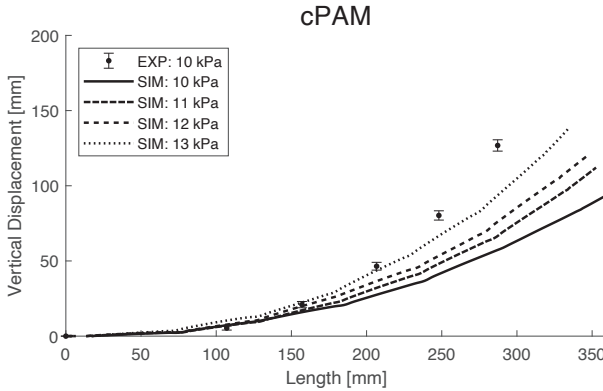


Fig. 5. FEA simulation values for the cPAM at 11, 12, and 13 kPa to test the hypothesis that the FEA has lower accuracy at partially buckled states.

the most stable, and the FEA corresponds to the experiments with over 96.7% accuracy for all pressures. The fabric model in Abaqus causes oscillations in the results that can be mitigated by controlling the simulation time step. The deformation amplitude is not affected, but the computational cost of the FEA increases with increasing time step. A judicious choice of time step and mass scaling will affect the run time and the oscillation frequency. We find that the oscillations always have the same amplitude, which corresponds to the experimental deformed state.

One particularly important value for the FEA accuracy is the mesh size. It affects the deformation range of an actuator significantly, especially for the cPAM and ePAM that principally rely on buckling for bending. In preliminary work, we simulated all actuators with mesh sizes ranging from 0.7 to 4 mm. While the ePAM and fPAM were not particularly sensitive to the change, the accuracy of the cPAM and ePAM increased by nearly 20%. The finer mesh size translates to deeper and more complex buckling patterns, which in turn increases the bending radius. However, run times also increase exponentially with mesh refinement, so our final mesh size is a compromise of accuracy and efficiency. Depending on whether a user is aiming to qualitatively understand the deformation mechanism or needs quantitative information to, say, design an IBR for a specific trajectory, the emphasis can be shifted by manipulating the mesh size.

Overall, the FEA results reported here are accurate, demonstrating that FEA is a promising tool for the design and deployment of IBRs. There are two differentiating factors between the actuators: the bending mechanism (geometry-based contraction or material-based contraction) and external or embedded actuator system. Combining geometric and embedded actuation yields the highest deformation range, but also the most buckling and inaccuracies for lower pressures. Material-based external actuation is the most accurate, but has the smallest range. These results can help roboticists decide on the most appropriate design for their case study. For example, if an IBR needs to follow a very tortuous path without interacting with its environment, the cPAM is the best choice. If an IBR needs to overcome only small obstacles and

uses the actuator mechanism mostly to steer its tip, an fPAM would be easier to implement.

The FEA approach is also an excellent tool to support IBR fabrication in general. The von Mises stress distribution can inform, for example, where a design is most likely to rupture. If the weld strength has been characterized, ruptures can be predicted and avoided through design or material changes, or by iterating on the weld parameters. Doing these iterations computationally rather than experimentally will save both time and materials, and reduce the length of the process significantly. No other IBR model published to date can provide this type of support, which is why we choose to make our model freely available online for others to use and to build on by, for example, including new types of actuators.

An additional advantage of using FEA modeling in IBR design is that very long IBR models can be easily built and tested virtually. Where other models have focused on mimicking the deformation of an IBR in empty space, with FEA interactions with the environment can be modeled by including additional steps and timed external loads. By building an environment virtually, the choice of actuator and general design can be optimized for specific applications or experimental obstacles that the IBR might encounter.

#### IV. CONCLUSION

This work validates a new approach of modeling pneumatically-actuated inflated beam soft robots, or IBRs, using FEA. Thanks to its *Dynamic, Explicit* formulation, the FEA accurately represents complex buckling patterns and anisotropic material models and is applicable to both geometry-based bending and material-based bending mechanisms. The model converges accurately for the four main types of pneumatic actuators currently used with IBRs.

A combination of buckling-based actuation and embedded actuator design result in the highest bending curve and deformation range. However, the stress singularities during buckling formation at lower pressures affect the model accuracy. Material-based deformation retains over 96.7% accuracy at all pressures, but has the smallest deformation potential.

The FEA approach proposed in this work can be adapted to achieve qualitative and quantitative results that streamline different stages of the IBR design process. This tool will be instrumental in producing more efficient IBRs both by avoiding ruptures or failures that create material and labor waste, and by tailoring actuator use and placement to specific applications.

#### REFERENCES

- [1] B. Sparrman, C. du Pasquier, C. Thomsen, S. Darbari, R. Rustom, J. Laucks, K. Shea, and S. Tibbits, "Printed silicone pneumatic actuators for soft robotics," *Additive Manufacturing*, vol. 40, no. 4, pp. 101860–101872, 2021.
- [2] C. du Pasquier, T. Chen, S. Tibbits, and K. Shea, "Design and Computational Modeling of a 3D Printed Pneumatic Toolkit for Soft Robotics," *Soft Robotics*, vol. 6, no. 5, pp. 657–663, 2019.
- [3] C. Duriez, "Control of elastic soft robots based on real-time finite element method," *IEEE International Conference on Robotics and Automation*, pp. 3982–3987, 2013.
- [4] L. H. Blumenschein, M. Koehler, N. S. Usevitch, E. W. Hawkes, D. C. Rucker, and A. M. Okamura, "Geometric Solutions for General Actuator Routing on Inflated-Beam Soft Growing Robots," *IEEE Transactions on Robotics*, vol. 38, no. 3, pp. 1820–1840, 2022.

- [5] R. Jitosho, S. Simon-Trench, A. M. Okamura, and B. H. Do, “Passive Shape Locking for Multi-Bend Growing Inflated Beam Robots,” in *IEEE International Conference on Soft Robotics (RoboSoft)*, 2023, pp. 1–6.
- [6] J. Hwee, A. Lewis, R. A. Bly, K. S. Moe, and B. Hannaford, “An Everting Emergency Airway Device,” *International Symposium on Medical Robotics*, pp. 1–7, 2021.
- [7] S. Voisembert, N. Mechbal, A. Riwan, and A. Ouassat, “Design of a Novel Long-Range Inflatable Robotic Arm: Manufacturing and Numerical Evaluation of the Joints and Actuation,” *Journal of Mechanisms and Robotics*, vol. 5, no. 4, pp. 1–9, 2013.
- [8] T. Takahashi, K. Tadakuma, M. Watanabe, E. Takane, N. Hookabe, H. Kajihara, T. Yamasaki, M. Konyo, and S. Tadokoro, “Eversion Robotic Mechanism with Hydraulic Skeleton to Realize Steering Function,” *IEEE Robotics and Automation Letters*, vol. 6, no. 3, pp. 5413–5420, 7 2021.
- [9] D. A. Haggerty, N. D. Naclerio, and E. W. Hawkes, “Hybrid Vine Robot with Internal Steering-Reeling Mechanism Enhances System-Level Capabilities,” *IEEE Robotics and Automation Letters*, vol. 6, no. 3, pp. 5437–5444, 2021.
- [10] L. T. Gan, L. H. Blumenschein, Z. Huang, A. M. Okamura, E. W. Hawkes, and J. A. Fan, “3D electromagnetic reconfiguration enabled by soft continuum robots,” *IEEE Robotics and Automation Letters*, vol. 5, no. 2, pp. 1704–1711, 2020.
- [11] M. M. Coad, L. H. Blumenschein, S. Cutler, J. A. Reyna Zepeda, N. D. Naclerio, H. El-Hussieny, U. Mehmood, J. H. Ryu, E. W. Hawkes, and A. M. Okamura, “Vine Robots: Design, Teleoperation, and Deployment for Navigation and Exploration,” *IEEE Robotics and Automation Magazine*, vol. 27, no. 3, pp. 120–132, 2020.
- [12] N. D. Naclerio and E. W. Hawkes, “Simple, low-hysteresis, foldable, fabric pneumatic artificial muscle,” *IEEE Robotics and Automation Letters*, vol. 5, no. 2, pp. 3406–3413, 2020.
- [13] R. Niityama, X. Sun, C. Sung, B. An, D. Rus, and S. Kim, “Pouch Motors: Printable Soft Actuators Integrated with Computational Design,” *Soft Robotics*, vol. 2, no. 2, pp. 59–70, 2015.
- [14] E. W. Hawkes, L. H. Blumenschein, J. D. Greer, and A. M. Okamura, “A soft robot that navigates its environment through growth,” *Science Robotics*, vol. 2, no. 8, pp. 3028–3035, 2017.
- [15] A. M. Kübler, S. U. Rivera, F. B. Raphael, J. Förster, R. Siegwart, and A. M. Okamura, “A Multi-Segment, Soft Growing Robot with Selective Steering,” *IEEE International Conference on Soft Robotics (RoboSoft)*, pp. 1–7, 2023.
- [16] J. D. Greer, T. K. Morimoto, A. M. Okamura, and E. W. Hawkes, “Series Pneumatic Artificial Muscles (sPAMs) and Application to a Soft Continuum Robot,” *IEEE International Conference on Robotics and Automation (ICRA)*, pp. 5503–5510, 2017.
- [17] T. Abrar, F. Putzu, A. Ataka, H. Godaba, and K. Althoefer, “Highly Manoeuvrable Eversion Robot Based on Fusion of Function with Structure,” *IEEE International Conference on Robotics and Automation (ICRA)*, pp. 7130–7136, 2021.
- [18] M. Smith, *ABAQUS/Standard User’s Manual, Version 6.14*. Dassault Systemes Simulia Corp, 2014.
- [19] A. M. Kübler, C. du Pasquier, A. Low, B. Djambazi, N. Aymon, J. Förster, N. Agharese, R. Siegwart, and A. M. Okamura, “A Comparison of Pneumatic Actuators for Soft Growing Vine Robots,” 2023. [Online]. Available: <https://arxiv.org/abs/2305.00967v1>
- [20] J. D. Greer, T. K. Morimoto, A. M. Okamura, and E. W. Hawkes, “A Soft, Steerable Continuum Robot That Grows via Tip Extension,” *Soft Robotics*, vol. 6, no. 1, pp. 95–108, 2019.
- [21] A. Tabiei, R. Tanov, and G. J. Simitses, “Numerical Simulation of Cylindrical Laminated Shells Under Impulsive Lateral Pressure,” *AIAA Journal*, vol. 37, no. 5, pp. 629–633, 2012.
- [22] A. Rostamijavanani, “Dynamic Buckling of Cylindrical Composite Panels Under Axial Compressions and Lateral External Pressures,” *Journal of Failure Analysis and Prevention*, vol. 21, no. 1, pp. 97–106, 2020.
- [23] J. Cao, R. Akkerman, P. Boisse, J. Chen, H. S. Cheng, E. F. de Graaf, J. L. Gorczyca, P. Harrison, G. Hivet, J. Launay, W. Lee, L. Liu, S. V. Lomov, A. Long, E. de Luycker, F. Morestin, J. Padoviskis, X. Q. Peng, J. Sherwood, T. Stoilova, X. M. Tao, I. Verpoest, A. Willems, J. Wiggers, T. X. Yu, and B. Zhu, “Characterization of mechanical behavior of woven fabrics: Experimental methods and benchmark results,” *Composites Part A: Applied Science and Manufacturing*, vol. 39, no. 6, pp. 1037–1053, 2008.
- [24] J. Launay, G. Hivet, A. V. Duong, and P. Boisse, “Experimental analysis of the influence of tensions on in plane shear behaviour of woven composite reinforcements,” *Composites Science and Technology*, vol. 68, no. 2, pp. 506–515, 2008.

## ACKNOWLEDGMENT

The authors thank Alexander Kübler for the development of the experimental procedure and the measurements performed with the sPAM/PM, cPAM, and fPAM.